

Tuning Breakdown-to-Coercive Field Ratio in Ultra-Thin Al_{1-x}Sc_xN Films via Reactive Nitrogen Atmosphere

Yinuo Zhang, Walter J. Smith, Giovanni Esteves, *Eric A. Stach**, *Thomas E. Beechem,** and Roy H. Olsson III*

Abstract—Al_{1-x}Sc_xN has attracted significant interest due to its large remnant polarization and low processing temperature when compared to other ferroelectric material systems. However, device dielectric failure before ferroelectric switching remains a critical limitation for AlScN-based memory devices. With the continuing trend toward device miniaturization, expanding the operating window is essential for next-generation memory development. In this work, we optimized the breakdown field (E_{BD}) and coercive field (E_C) in ultra-thin Al_{1-x}Sc_xN films by controlling defect density via adjustment of nitrogen gas flow during sputter deposition. The characteristic breakdown field, E_{BD} , was evaluated using Weibull statistics, yielding optimal characteristic breakdown fields of 12.47 MV/cm (E_{BD}^+) and -12.63 MV/cm (E_{BD}^-) for samples deposited under 27.5 sccm N₂ flow. The minimum E_C was achieved at a nitrogen flow of 25 sccm and increased for higher gas flows, a trend that is opposite to previous reports in much thicker films. The highest E_{BD}/E_C ratio of 2.25 occurred at 27.5 sccm, effectively expanding the operational window. Using a combination of X-ray diffraction and photoluminescence spectroscopy to study changes in crystal orientation and defects, device performance can be tuned by controlling the point defect concentration in the ultra-thin film via adjusting the sputtering N₂ process gas flow rate.

Index Terms—Al_{1-x}Sc_xN, ferroelectric memory, Weibull distribution, photoluminescence, defect density

I. Introduction

Ferroelectric aluminum scandium nitride (Al_{1-x}Sc_xN) has emerged as a promising material for next-generation non-volatile memories, owing to its high spontaneous polarization,

This work is supported in part by Army/ARL via the Collaborative for Hierarchical Agile and Responsive Materials (CHARM) under cooperative agreement W911NF-19-2-0119. This work was performed in part at the Singh Center for Nanotechnology at the University of Pennsylvania, a member of the National Nanotechnology Coordinated Infrastructure (NNCI) network, which is supported by the National Science Foundation (Grant NNCI-2025608). Additional support for the X-ray diffraction facility at the University of Pennsylvania was provided by the NSF via the Materials Research Science and Engineering Center (MRSEC) (DMR-2309043). This research was primarily/partially supported by NSF through the University of Pennsylvania Materials Research Science and Engineering Center (MRSEC) (DMR-2309043). W.S. and T.B. acknowledge funding from Sandia National Laboratories University Partnerships program administered through Laboratory

scalability, and compatibility with complementary metal-oxide-semiconductor (CMOS) back-end-of-line (BEOL) processes.[1-5] These attributes make Al_{1-x}Sc_xN particularly attractive for integration into ultra-scaled ferroelectric devices. As the demand for minimizing device dimensions intensifies, maintaining and improving robust ferroelectric performance in ultra-thin Al_{1-x}Sc_xN films with thickness < 20 nm has become increasingly critical.[6-8] Various approaches, such as interfacial engineering, impurity doping, and defect density control, have been explored to improve and optimize ferroelectricity at reduced thicknesses.[9-12] Nitrogen gas flow is a critical processing parameter that directly influences film stoichiometry and crystallinity and is known to influence the ferroelectric properties in thicker Al_{1-x}Sc_xN films.[13-15] Despite this, the role of nitrogen gas (N₂) flow during co-sputtering deposition on the ferroelectric behavior of ultra-thin Al_{1-x}Sc_xN has not been investigated.

For example, *Yang et al.* demonstrated that the crystalline quality of 2 μm thick *c*-axis oriented AlScN deposited by reactive pulsed Direct Current (DC) magnetron sputtering could be optimized by changing N₂/Ar sputtering atmosphere, which also affected the film electrical properties such as resistivity.[16] The electromechanical properties are also influenced by reactive gas concentration in thicker Al_{1-x}Sc_xN.[17] Even with this clear dependency between reactive gas environment and the electrical response in thicker Al_{1-x}Sc_xN, its impact on key device performance metrics such as coercive field (E_C), breakdown field (E_{BD}), and their ratio (E_{BD}/E_C) in the ultra-thin (~10 nm) thickness regime characteristic of scaled memory devices remains unclear. Moreover, a mechanistic description linking the N₂ flow rate to material changes in the AlScN has yet to be established. Here, we examine the impact of N₂ gas flow environment on the electrical characteristics of

Directed Research and Development (LDRD). Yinuo Zhang and Roy H. Olsson are with the Electrical Systems and Engineering Department, University of Pennsylvania, Philadelphia, PA 19104 USA. (e-mail: rolsson@seas.upenn.edu).

Eric A. Stach is with the Material Science and Engineering Department, University of Pennsylvania, Philadelphia, PA 19104 USA. (e-mail: stach@seas.upenn.edu).

Walter J. Smith and Thomas J. Beechem are with the School of Mechanical Engineering, Purdue University and Birck Nanotechnology Center, West Lafayette, IN 47907 USA, (e-mail: tbeechem@purdue.edu).

Giovanni Esteves is with the Microsystems Engineering, Science and Applications, Sandia National Laboratories, Albuquerque, New Mexico, USA.

ultra-thin Al_{1-x}Sc_xN and assess the material changes causing the observed changes in device characteristics.

The reactive gas environment can influence the point defect concentration (*e.g.*, nitrogen (N) or metal (M) vacancies) in the film, which impacts device performance. Vacancies in AlN-films, for example, have been reported to modulate the bandgap and conductivity, increase leakage current, and cause ferroelectric switching fatigue.[18-20] With respect to Al_{1-x}Sc_xN in particular, a recent study of a 100 nm thick film suggested that a reduction in N-vacancies induced by a N-rich TiN bottom electrode improved ferroelectric performance.[21] From this evidence, we hypothesize that N and metal (*i.e.*, Al or Sc) vacancy density in ultra-thin (~10 nm) Al_{1-x}Sc_xN films can be tuned by varying the N₂ partial pressure while removing Ar gas during the co-sputtering process, leading to corresponding improvement in the electrical properties of the ferroelectric Al_{1-x}Sc_xN material.

To test this hypothesis, E_C , E_{BD} and their ratio (E_{BD}/E_C) were measured as a function of N₂ gas flow during synthesis to assess the degree to which this process parameter might affect the switching performance, operational window and device reliability. These parameters are particularly important for practical device design in ultra-thin film systems, where increased leakage current and higher switching barriers present significant challenges.[22-24]

Beyond assessing device characteristics, material alterations induced by changes in the reactive gas environment were also examined via photoluminescent studies capable of tracking changes in defects. Using this approach, moderate N₂ flow rates were found to improve the E_{BD} and E_{BD}/E_C ratio. This performance improvement correlated with an increase in the PL signature associated with N interstitials defects suggesting a lowering of N- vacancy concentration correlated with the higher performance. However, as the N₂ flow rate was further increased, the overall PL intensity increased, suggesting an increase in overall defect concentration that correlates with measured reductions in the E_{BD} and E_{BD}/E_C .

The paper is organized as follows. In Section II we present the experimental details, including the film growth conditions, device fabrication process, material and electrical characterization procedures. In Section III, we present the results and correlate the film growth orientation, device electrical properties, and PL results to elucidate the impact of defects on ferroelectric failure and switching performance.

II. EXPERIMENTAL DETAILS

A. Film Growth, Device Fabrication and Characterization

Ultra-thin Al/Al_{0.68}Sc_{0.32}N/Al (50 nm/~10 nm/50 nm) film stacks were deposited on 4 inch *c*-axis oriented sapphire wafers using the target powers, temperature, time and target-to-substrate distance reported in Zhang *et al.*[9] and summarized in Table 1. The N₂ gas flow was held constant during each individual deposition. The entire Al/Al_{0.68}Sc_{0.32}N/Al was deposited without vacuum break to prevent surface oxidation of the Al_{0.68}Sc_{0.32}N and Al bottom electrode as reported by Zheng

et al.[7] The film stacks for photoluminescence analysis are sapphire/Al(50 nm)/ Al_{0.68}Sc_{0.32}N (200nm)/AlN(20nm). The 200 nm Al_{0.68}Sc_{0.32}N films were grown with the same target powers but each sample was grown under a different N₂ gas flow from 20 sccm to 40 sccm (20, 25, 30, 35, 40 sccm) followed by a 20 nm AlN deposition to prevent oxidation of Al_{0.68}Sc_{0.32}N. Ferroelectric capacitors (FeCaps) were fabricated using the process reported in Zhang *et al.*[9]

Table 1. Deposition parameters of ultra-thin Al_{0.68}Sc_{0.32}N

Parameter	Value/Condition
Substrate	Sapphire
Target power density (W/cm ²)	Al: 12.7 W/cm ² Sc: 8.32 W/cm ²
Temperature (°C)	350
Deposition Time (s)	42.5
Base Pressure (mbar)	~5×10 ⁻⁸
Target-to-substrate distance (mm)	103.3
N ₂ gas flow (sccm)	22.5, 25, 27.5, 30, 35, 40

B. X-Ray Diffraction

X-ray diffraction (XRD) and X-ray reflectivity (XRR) were used to evaluate AlScN film thickness and texture using a PANalytical X'Pert³ MRD diffractometer equipped with a monochromatic beam and PIXcel detector. θ - 2θ scans were acquired to determine the out-of-plane orientation and lattice spacing of the AlScN and Al layers. Rocking curve (ω -scan) measurements of the AlScN (0002) reflection were conducted to assess crystallographic texture, where narrower full width at half maximum (FWHM) values indicate stronger alignment. The (0002) rocking curve peaks were fit to extract FWHM values for sample comparison, while XRR data were modeled in GSAS-II to fit Kiessig fringes and obtain film thickness.

C. Electrical Measurement

The breakdown field values were collected by performing 25 kHz (pulse width = 2×10⁻⁵ s) monophasic triangular pulses on 20 spatially distributed capacitors across the wafer. The positive electric breakdown (E_b^+) and negative electric breakdown fields (E_b^-) were obtained by applying pulses with opposite electric field polarizations. The coercive fields were obtained by 25 kHz biphasic triangular Positive-Up-Negative-Down (PUND) pulses,[23] on 5 different capacitors spatially distributed across the wafer. All the electrical tests were conducted using a Keithley 4200-SCS system.

D. Photoluminescence analysis

The evolution of defects were studied via photoluminescence spectroscopy (PL) on films with varying N₂ flow during film growth. PL was collected in air on a WITec Alpha300R confocal microscope using a 405 nm laser at 0.10 mW across a diffraction limit spot size of ~450 nm. Scattered light was collected using a UHTS VIS 600 spectrometer with a spectral resolution of less than 0.01 eV. Fitting of the spectra and assignment of features was performed using methods analogous to that employed in [20].

III. RESULTS AND DISCUSSION

A. X-Ray Diffraction and X-Ray Reflectometry Analysis

The crystallographic orientation of the films was studied using X-ray diffraction (XRD). As shown in **Figure 1a**, a 2 θ scan from 30° to 40° was performed on Al/Al_{0.68}Sc_{0.32}N/Al film stacks. The (0002) out-of-plane diffraction peak of Al_{0.68}Sc_{0.32}N was clearly identified at approximately 35.5°, while a highly textured Al(111) peak was observed near 38.5°. To further evaluate the *c*-axis orientation, rocking curve scans were conducted for each sample, as shown in Figure 1b. The full-width at half-maximum (FWHM) values were extracted from these curves with their dependence on reactive N₂ flow rate is exhibited in Figure 1c. Overall, the FWHM values increase with increasing N₂ flow rate, suggesting a lower quality of *c*-axis oriented AlScN except the film grown under 35 sccm N₂ which shows a significant increase in the FWHM and corresponds to the device with the poorest dielectric breakdown performance, as will be discussed in Section B. In contrast, the film deposited under the lowest N₂ flow condition exhibited the narrowest FWHM, indicating a better *c*-axis alignment of the Al_{0.68}Sc_{0.32}N (0002).

To gain information on film thickness for property analysis, X-ray Reflectometry (XRR) measurements were conducted on each layer stack. The thickness of Al_{0.68}Sc_{0.32}N is summarized in **Table 2**. The thickness decreases with increasing N₂ gas flow, even though all films were deposited for the same duration, an effect attributed to increased scattering at higher flow rates. The thickness of the ultra-thin Al_{0.68}Sc_{0.32}N films ranged from 9.6 nm to 11.7 nm.

B. Breakdown and Failure Analysis

Subsequent to thin film deposition and structural characterization, the ferroelectric performance and device reliability were studied. Electrical measurements were performed on ferroelectric capacitors with a 4 μ m diameter. A cross-sectional diagram of the capacitor structure is depicted in **Figure 2**.

First, the impact of N₂ flow on breakdown field was investigated. The Weibull distribution of the FeCap breakdown fields for the films deposited under different N₂ flows is plotted in **Figure 3a** and **Figure 3b**. The Weibull probability distribution is commonly used to describe the statistical distribution of electron trap density that leads to dielectric failure [25] and is widely employed to assess the lifetime of

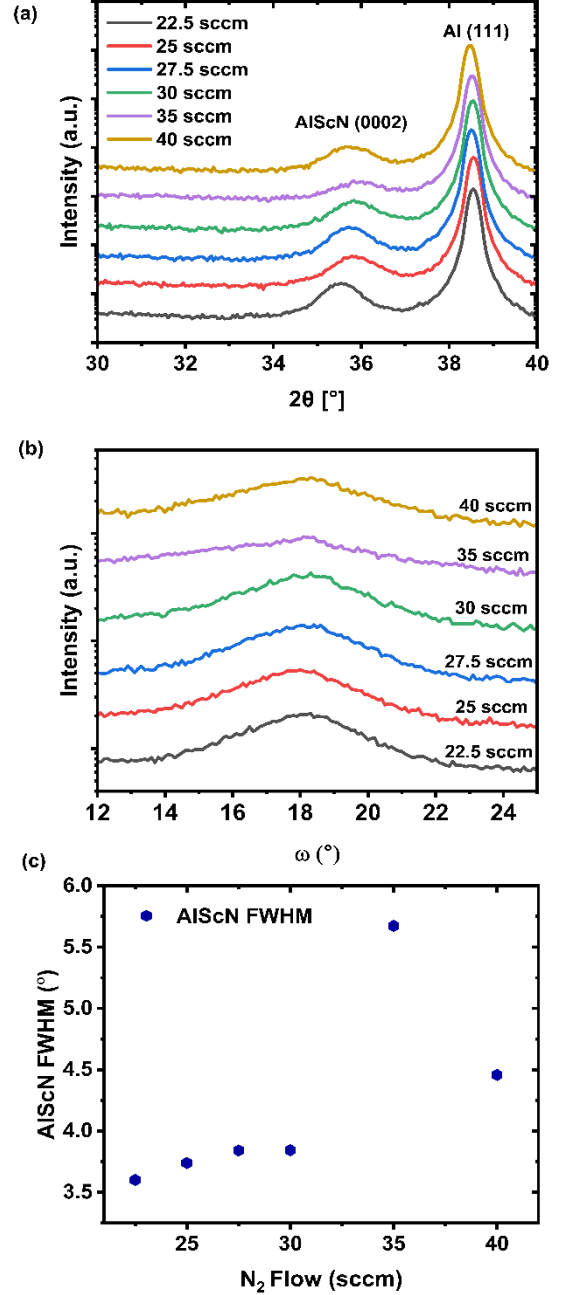


Figure 1. XRD measurement of thin film stacks. (a). 2 θ scan of Al/Al_{0.68}Sc_{0.32}N/Al from 30° to 40° with (0002) Al_{0.68}Sc_{0.32}N and (111) Al labeled. (b). Rocking curve scan for the (0002) Al_{0.68}Sc_{0.32}N films deposited under different N₂ flow. (c) FWHM obtained by Pearson VII for ultra-thin Al_{0.68}Sc_{0.32}N films by varying the reactive N₂ gas flow.

electronic devices and to predict the reliability of manufactured products.[26-28] The relationship between the failure probability and experimental breakdown field data points is described by equation (1),

$$F = 1 - \exp\left(-\left(\frac{E_b}{E_{BD}}\right)^\beta\right) \quad (1)$$

where E_b is the experimental breakdown field data points. Each data point was obtained by applying a unipolar, 25 kHz

triangular pulse with a maximum voltage equal to +40 V. The breakdown failure of the device was evaluated by both applying positive and negative monopolar triangular waveforms. Twenty capacitors spatially distributed across the full area of a wafer piece were selected randomly as the breakdown test subjects. E_{BD} is the breakdown field where the failure probability is 63% (also called characteristic breakdown field). [28, 29] In this work, we used E_{BD} to compare the breakdown properties of each device and calculated $E_{\text{BD}}/E_{\text{C}}$ to evaluate the window of operation and endurance potential.[30, 31] β is the shape factor of the Weibull distribution plot, which describes the uniformity the breakdown field.[25, 32]

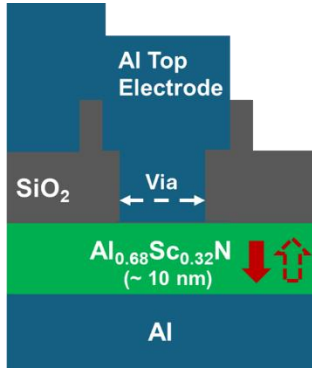


Figure 2. Cross -section schematic of FeCap structure. The dashed arrow in the $\text{Al}_{0.68}\text{Sc}_{0.32}\text{N}$ layer represents the ferroelectric dipole direction after deposition while the solid red arrow represents the direction of the dipole after switching.

Characteristic breakdown values (E_{BD}^+ and E_{BD}^-) as a function of N_2 flow are plotted in **Figure 3c**. The FeCaps fabricated from the ultra-thin film deposited under 27.5 sccm N_2 exhibit the highest E_{BD} under both pulse polarities (12.47 MV/cm and -12.63 MV/cm). Under positive triangular wave pulses, E_{BD} decreased with further increases in N_2 flow. For instance, at 40 sccm, E_{BD} dropped to 9.9 MV/cm, the lowest value observed among all tested devices. While under negative pulses, a pronounced reduction could also be observed as N_2 flow increased beyond 27.5 sccm, but the absolute E_{BD}^- values starts to increase again after reaching a minimum for the 35 sccm N_2 sample.

To evaluate the breakdown uniformity, the shape factor, β , was extracted from each Weibull Distribution and is summarized in **Table 2**. All devices under positive and negative pulses exhibit shape factors greater than 1, suggesting that the failure probability increases with higher electric field (E_{b}), consistent with a wear-out breakdown mechanism caused by high-voltage pulse stress.[33, 34] Furthermore, the FeCaps fabricated from the ultra-thin AlScN film grown under 27.5 sccm N_2 have the highest shape factor ($\beta^+ = 35.3$, $\beta^- = 16.50$), producing the most steep Weibull curve and indicating a tight breakdown field distribution with excellent device-to-device consistency. In contrast, the lowest β^+ and β^- generated by the FeCaps were observed in the ferroelectric $\text{Al}_{0.68}\text{Sc}_{0.32}\text{N}$ layer deposited at 40 sccm N_2 and 35 sccm N_2 flow respectively, indicating a broad breakdown distribution and a wider range of breakdown fields, especially for applied voltage pulses with positive

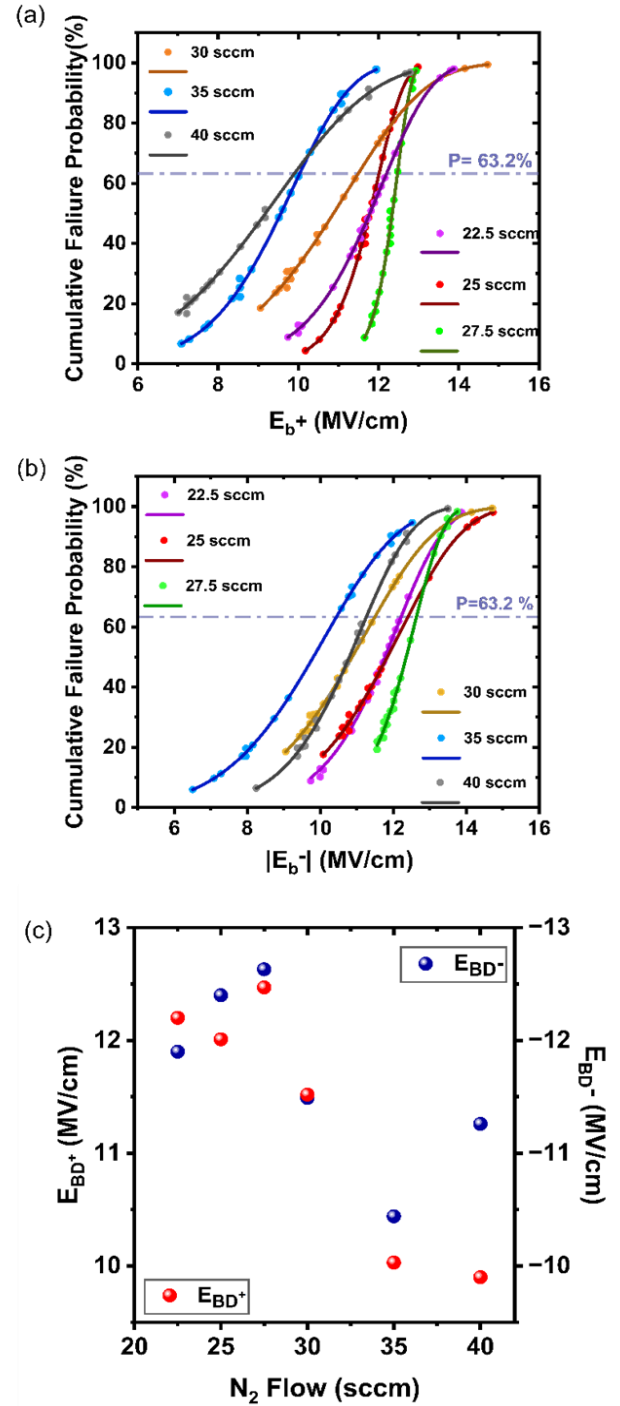


Figure 3. Breakdown analysis of $\text{Al}_{0.68}\text{Sc}_{0.32}\text{N}$ FeCaps (a) Weibull distribution of FeCap breakdown when applying positive triangular pulses. (b) Weibull distribution of FeCap breakdown when applying negative triangular pulses. (c) E_{BD}^+ and E_{BD}^- versus N_2 gas flow

polarity. The E_{BD} and shape factors of the devices made from different sputtering atmospheres are summarized in **Table 2**. Overall, the 27.5 sccm N_2 flow condition yielded both the highest breakdown field and the most concentrated failure distribution. Moreover, devices grown under higher N_2 flow rates (i.e., 35 sccm and 40 sccm N_2), which generated higher XRD-derived FWHM values and thus less c-axis oriented AlScN (see Figure 1b and 1c) exhibited poorer breakdown

performance. Simply stated, greater disorder in the films correlated with reduced breakdown performance and uniformity in device response, as exemplified by the lower β for these films (see **Table 2**). This behavior suggests increased defect activity, which is supported by the PL-measurements discussed in Section D.

Table 2. Summary of the electrical performance of FeCaps deposited under different N₂ flows.

N ₂ Flow (sccm)	22.5	25	27.5	30	35	40
Thickness (nm)	11.7	11.4	10.9	10.6	10.4	9.6
E _{BD+} (MV/cm)	12.2	12.0	12.5	11.5	10.0	9.9
E _{BD-} (MV/cm)	-11.9	-12.4	-12.6	-11.5	-10.4	-11.3
β^+ (E _{BD+})	10.6	18.7	35.3	6.6	7.7	4.9
β^- (E _{BD-})	8.2	8.0	16.5	6.6	5.9	8.7
E _c (MV/cm)	-5.7	-5.5	-5.7	-5.7	-5.8	-6.0
E _{BD} /E _c	2.1	2.3	2.2	2.0	1.8	1.9

C. Coercive Field Measurements and Device Operating Window Evaluation

The E_c of films deposited with different N₂ flow rates was investigated via triangular Positive-Up-Negative-Down (PUND) tests. A 25 kHz triangular Current density-Electric field (JE) JE-PUND analysis was employed to compensate leakage current and isolate the ferroelectric switching response.[9, 35] To minimize selection bias, five FeCaps with spatially distributed locations on each wafer piece were selected for E_c measurements. The average values and corresponding error bars are presented in **Figure 4**.

The positive coercive field could not be clearly identified due to measurement limitations and increased leakage during the Nitrogen-polar to Metal-polar polarization switching of the ultra-thin films. Therefore, only the negative coercive field was considered for comparative analysis across different N₂ flow conditions. As shown in **Figure 4**, although the film grown under 22.5 sccm N₂ exhibited a slightly higher E_c, a clear increasing trend in coercive field was observed starting from 25 sccm N₂ flow. This is counter to the trend observed in thicker films (> 50 nm) where an increased N₂ flow led to a more tensile film stress and a lower coercive field. [3, 17].

To better evaluate the device's operational window, the absolute value of E_{BD}/E_c with N₂ flow during growth is plotted in **Figure 5**, where the average E_c was selected to calculate E_{BD}/E_c. In the ultra-thin film system, a maximum E_{BD}/E_c = 2.25 was obtained when the N₂ flow was 25 sccm. The best operation window occurs under the same conditions as that which leads to the greatest endurance potential. At lower N₂ flows (22.5 sccm), the ratio was slightly reduced. In contrast, a sharp decline in E_{BD}/E_c value was observed when the N₂ concentration exceeded 27.5 sccm, which contradicts the trend reported by *Yang et al.* [21] measured in much thicker films. At

35 sccm N₂ flow, the ratio dropped to 1.80, the lowest value recorded in this study. The higher XRD FWHM value of *c*-axis oriented AlScN film grown under 35 sccm N₂ flow corresponds to the lowest E_{BD}⁻, suggesting that the quality of the film plays

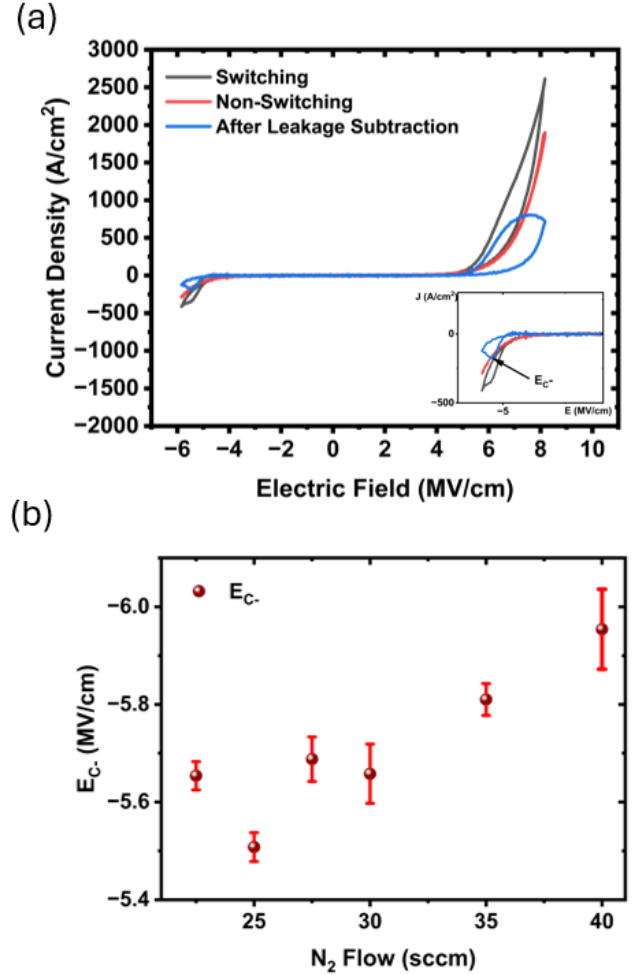


Figure 4. (a) JE-PUND measurement of 25 sccm N₂ flow rate AlScN showing switching, non-switching and JE loop after leakage subtraction; Inset is the zoom-in negative JE loop of E_c location; (b) Negative E_c versus N₂ gas flow

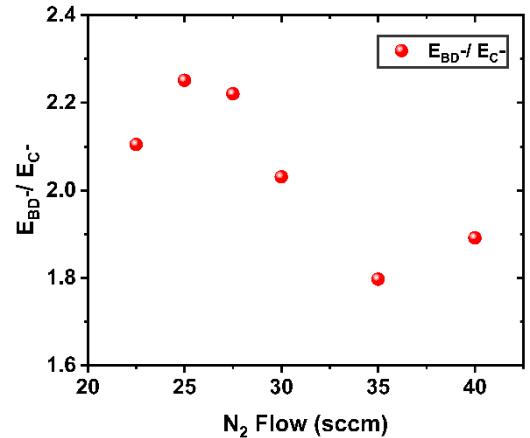


Figure 5. E_{BD}⁻/E_c⁻ versus N₂ flow

a role in inducing the dielectric failure. The E_{BD}/E_C values each of device have been summarized in **Table 2**.

D. Defect Analysis Using Photoluminescence

To understand the underlying mechanism for the E_{BD} and E_C trends as a function of N_2 flow during film growth, photoluminescence spectroscopy of the Al_{0.68}Sc_{0.32}N films was conducted and the spectra were analyzed via curve fitting. Photoluminescence is a three step-process, requiring absorption of incident photons, scattering through phonons or other means, and subsequent radiative recombination, which is measured as transitions that occur between the conduction band, valence band, and defects. Utilization of sub-bandgap excitation preferentially samples from defects as it prohibits band-to-band absorption for the visible laser used for excitation here.

Changes in the PL-spectra with increasing N_2 flow are provided in **Figure 6a** along with a representative fit used to assess the transitions giving rise to the signal (**Figure 6b**). Fitting was accomplished using a summation of four Gaussian functions revealing transitions having energies of 1.84 ± 0.10 eV, 1.95 ± 0.07 eV, 2.45 ± 0.07 eV, and 2.65 ± 0.03 eV. The linewidths (i.e. full-width at half-maximum, FWHM) for these transitions were 0.22 ± 0.05 eV, 0.49 ± 0.09 eV, 0.33 ± 0.06 eV, and 0.17 ± 0.03 eV.

As N_2 flow increases, the intensity of the 1.95 eV peak increases drastically while the intensity of the 2.45 eV and 2.65 eV peaks remain relatively constant, as shown in **Figure 7**. The intensity of the 1.84 eV, meanwhile, exhibits a non-monotonic dependence transitioning from a maximum between 20 sccm and 30 sccm, before subsequently decreasing. This non-monotonic behavior in the 1.84 eV feature is qualitatively similar to that observed both in the dependence of breakdown field (**Figure 3c**) and operation window (**Figure 5**) suggesting a link between this defect and overall performance.

To gain insight into the origin of this signal, we note that the formation energy, and thus the concentration of defects changes as the growth becomes increasingly N-rich. For example, increasing N during growth will decrease the number of N vacancies (V_N) and O substitutional defects (O_N). [36, 37] On the other hand, it will increase the probability of forming nitrogen interstitials, the number of metal vacancy defects (V_{Al} , V_{Sc}) and associated complexes consisting of these vacancies with any residual oxygen (i.e., oxygen defect complexes). [38] Recognizing this, changes in PL intensity with N_2 flow likely are linked to variations in these particular defects even as definitive assignment is quite difficult because the exact positions of many defects within the bandgap of AlScN remains unknown.

With this perspective, we can speculate that the constant increase in intensity for the transition at 1.95 with N_2 -flow is likely caused by an increase in those defects whose formation energy is most affected, namely the nitrogen interstitial defects (N_i) and/or metal vacancies. [19, 36] This type of N_i point defect is likely the key factor responsible for the rising E_C with the

increasing process N_2 gas flow (**Figure 7a** and **7b**). Interestingly, the E_C change of the ultra-thin Al_{1-x}Sc_xN film generally follows a linear trend with the energy transit intensity of 1.95 eV as shown in **Figure 7b**, indicating the correlation of defect density change tendency and ferroelectric switching energy barrier in the ultra-thin film system. Point defects are regarded as pinning sites during the domain wall motion in ferroelectric material systems. [39, 40] An increase in defects would, therefore, be expected to increase the coercive fields. However, their exact impact on ultra-thin AlScN film ferroelectric switching barrier remains unknown.

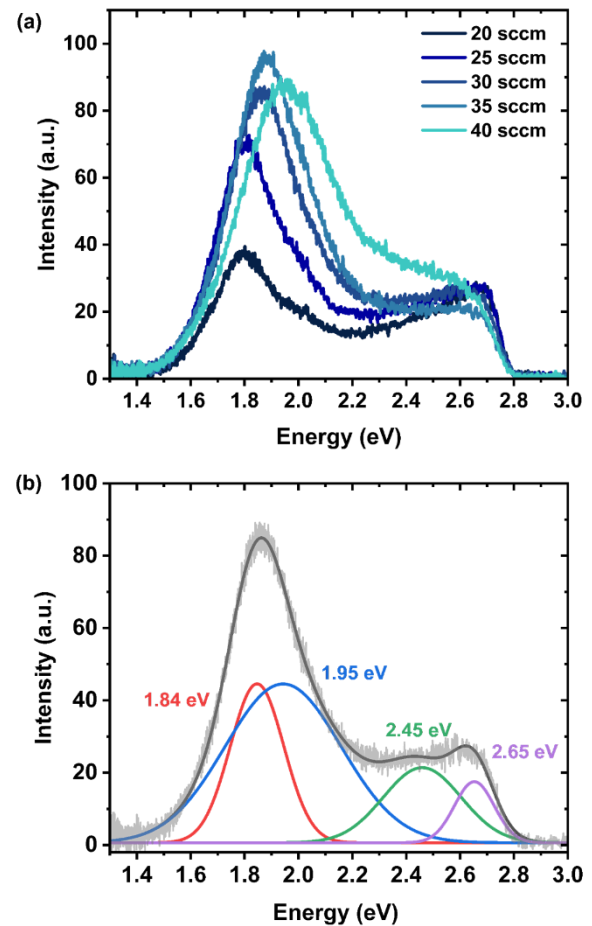


Figure 6. Photoluminescence spectrum of Al_{0.68}Sc_{0.32}N. (a) Signature peak intensity change vs. increasing N_2 flow rate. (b) Raw data of Al_{0.68}Sc_{0.32}N at 30 sccm N_2 flow with accompanying spectral fit comprised of four Gaussian line shapes.

The lower energy mode near 1.84 eV meanwhile is consistent with the presence of defect complexes composed of a metal vacancy interacting with residual oxygen (i.e., an O-complex).[38, 41] This deduction is based on knowledge that there is likely a small—but non-zero—concentration of oxygen in the films. This could be attributed to the replacement tendency of N by O during the film deposition.[42, 43] Furthermore, at low concentrations, even at low base pressures ($< 5 \times 10^{-8}$ mbar), oxygen defects are known to almost always

“find” metal vacancies to pair with in AlN. [19] The non-monotonic response with N₂-flow suggests that the increasing amount of metal vacancies form O-complexes until the residual oxygen is fully utilized.[41] Regardless, the presence of either of these defects is associated with a reduction in N-vacancies.

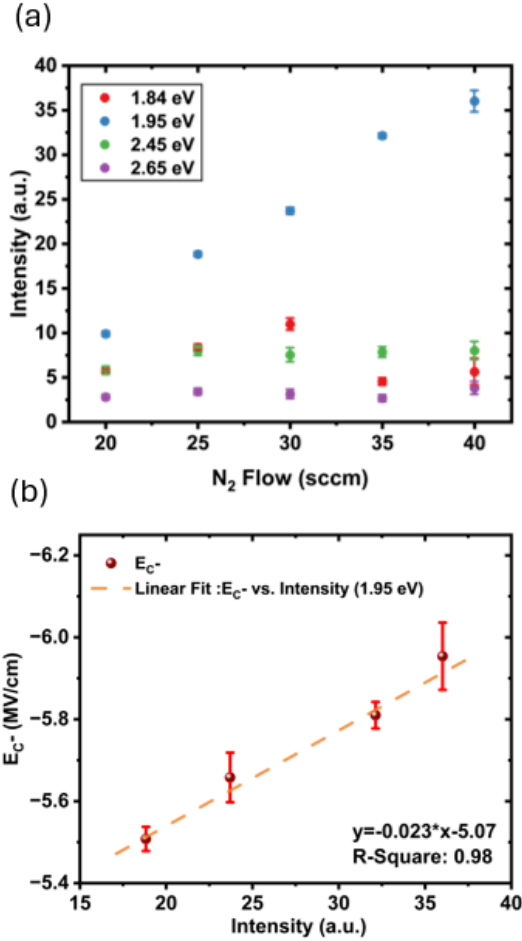


Figure 7. Energy transition correlates with E_C change (a) Intensity of the different transitions in the Al_{0.68}Sc_{0.32}N films. The intensity of the peak at 1.95 eV increases steadily as N₂ flow increases while the intensity of the peak at 1.84 eV is a maximum at 30 sccm N₂. (b) E_C vs. Energy Transition Intensity (1.95 eV) with a linear fitting.

The PL data, therefore, taken together with the E_C and E_{BD} data, suggests that a higher N₂ flow during film growth may decrease the number of N vacancies, resulting in an increase in E_C with increasing N₂ flow. At higher N₂ flows, above 27.5 sccm, the density of other defects (at 1.84 eV) increases, which reduces the breakdown field. For example, even though having similar FWHM values, the film grown under 30 sccm N₂ has lower breakdown strength than the film grown under 27.5 sccm because of the higher concentration of the defect at 1.84 eV. Taken in aggregate, the PL highlights how the defect environments is tightly intertwined with the ultimate performance of the device.

IV. CONCLUSION

In summary, we tuned the ferroelectric performance of ultra-thin AlScN capacitors by manipulating the processing N₂ gas flow to adjust the defect concentration. The breakdown field strength reached its maximum for an N₂ gas flow of 27.5 sccm. AlScN films with degraded c-axis texture indicated by higher XRD FWHM also exhibited lower dielectric breakdown. Interestingly, the coercive field increased with the increase in N₂ gas flow, which follows a opposite trend when compared to prior publications in thicker AlScN films. The E_{BD}/E_C was optimized to 2.25 under a 25 sccm N₂ flow. To better understanding how the point defects impact the ferroelectricity and dielectric failure, photoluminescence spectroscopy was performed on a series of thicker films sputtered under the same conditions. Photoluminescence analysis indicates that under N-rich conditions N_i related-defect energy transitions become more pronounced, exhibiting the same increasing trend of E_C with N₂ gas flow. Even though exhibiting similar FWHM, the appearance of O-complexes leads to a lower breakdown strength at 30 sccm N₂ process gas flow when comparing to the film grown under 27.5 sccm N₂ flow. The degree of c-axis orientation plus the point defects density contributes to the observed reduction in breakdown strength as well as the variation of E_{BD}/E_C. These findings offer new understanding of the relationship between film texture, point defects and the reliability of AlScN-based ferroelectric memory devices.

ACKNOWLEDGEMENT

Sandia National Laboratories is a multi-mission laboratory managed and operated by National Technology & Engineering Solutions of Sandia, LLC (NTESS), a wholly owned subsidiary of Honeywell International Inc., for the U.S. Department of Energy’s National Nuclear Security Administration (DOE/NNSA) under contract DE-NA0003525. This written work is authored by an employee of NTESS. The employee, not NTESS, owns the right, title and interest in and to the written work and is responsible for its contents. Any subjective views or opinions that might be expressed in the written work do not necessarily represent the views of the U.S. Government. The publisher acknowledges that the U.S. Government retains a non-exclusive, paid-up, irrevocable, world-wide license to publish or reproduce the published form of this written work or allow others to do so, for U.S. Government purposes. The DOE will provide public access to results of federally sponsored research in accordance with the DOE Public Access Plan.

V. REFERENCES

- [1] K.-H. Kim *et al.*, "Multistate, ultrathin, back-end-of-line-compatible AlScN ferroelectric diodes," *ACS nano*, vol. 18, no. 24, pp. 15925-15934, 2024.
- [2] Y. Zhang, Q. Zhu, B. Tian, and C. Duan, "New-generation ferroelectric AlScN materials," *Nano-Micro Letters*, vol. 16, no. 1, p. 227, 2024.
- [3] S. Fichtner, N. Wolff, F. Lofink, L. Kienle, and B. Wagner, "AlScN: A III-V semiconductor based ferroelectric," *Journal of Applied Physics*, vol. 125, no. 11, 2019.
- [4] R. Mizutani *et al.*, "Thickness scaling of (Al_{0.8}Sc_{0.2})N films with remanent polarization beyond 100 $\mu\text{C cm}^{-2}$ around 10 nm in thickness," *Applied Physics Express*, vol. 14, no. 10, p. 105501, 2021.
- [5] D. Wang *et al.*, "An epitaxial ferroelectric ScAlN/GaN heterostructure memory," *Advanced Electronic Materials*, vol. 8, no. 9, p. 2200005, 2022.
- [6] G. Schönweger *et al.*, "In - grain ferroelectric switching in sub-5 nm thin Al_{0.74}Sc_{0.26}N films at 1 V," *Advanced Science*, vol. 10, no. 25, p. 2302296, 2023.
- [7] J. X. Zheng *et al.*, "Ferroelectric behavior of sputter deposited Al_{0.72}Sc_{0.28}N approaching 5 nm thickness," *Applied Physics Letters*, vol. 122, no. 22, 2023.
- [8] C. Leblanc *et al.*, "Low-voltage Ferroelectric Field-Effect Transistors with Ultrathin Aluminum Scandium Nitride and 2D channels," *arXiv preprint arXiv:2504.07271*, 2025.
- [9] Y. Zhang *et al.*, "Coercive Field Reduction in Ultrathin Al_{1-x}Sc_xN via Interfacial Engineering with a Scandium Electrode," *arXiv preprint arXiv:2506.10169*, 2025.
- [10] M. Gremmel, C. Prakash Savant, D. Bhattacharya, G. Schönweger, D. Jena, and S. Fichtner, "The effect of boron incorporation on leakage and wake-up in ferroelectric Al_{1-x}Sc_xN," *Journal of Applied Physics*, vol. 137, no. 24, 2025.
- [11] Q. Wang *et al.*, "Understanding effect of distortions and vacancies in wurtzite AlScN ferroelectric memory materials: Vacancy-induced multiple defect state types and relaxation dependence in transition energy levels," *AIP Advances*, vol. 12, no. 12, 2022.
- [12] C. Skidmore *et al.*, "Sputtered ferroelectric aluminum scandium boron nitride (Al_{1-x-y}B_xSc_yN)/n-GaN heterostructures," *Journal of Applied Physics*, vol. 138, no. 1, 2025.
- [13] M. Signore *et al.*, "Low temperature sputtering deposition of Al_{1-x}Sc_xN thin films: Physical, chemical, and piezoelectric properties evolution by tuning the nitrogen flux in (Ar+ N₂) reactive atmosphere," *Journal of Applied Physics*, vol. 135, no. 12, 2024.
- [14] K. Kusaka, D. Taniguchi, T. Hanabusa, and K. Tominaga, "Effect of sputtering gas pressure and nitrogen concentration on crystal orientation and residual stress in sputtered AlN films," *Vacuum*, vol. 66, no. 3-4, pp. 441-446, 2002.
- [15] M. K. Sandager, C. Kjeldse, and V. Popok, "Growth of thin AlN films on Si wafers by reactive magnetron sputtering: Role of processing pressure, magnetron power and nitrogen/argon gas flow ratio," *Crystals*, vol. 12, no. 10, p. 1379, 2022.
- [16] J.-c. Yang, X.-q. Meng, C.-t. Yang, and W.-j. Fu, "Influence of N₂/Ar-flow ratio on crystal quality and electrical properties of ScAlN thin film prepared by DC reactive magnetron sputtering," *Applied surface science*, vol. 282, pp. 578-582, 2013.
- [17] R. Beaucejour, V. Roebisch, A. Kochhar, C. G. Moe, M. D. Hodge, and R. H. Olsson, "Controlling residual stress and suppression of anomalous grains in aluminum scandium nitride films grown directly on silicon," *Journal of Microelectromechanical Systems*, vol. 31, no. 4, pp. 604-611, 2022.
- [18] R. Wang *et al.*, "Wurtzite AlScN/AlN Superlattice Ferroelectrics Enable Endurance Beyond 10¹⁰ Cycles," *arXiv preprint arXiv:2506.22212*, 2025.
- [19] J.-M. Mäki *et al.*, "Identification of the V Al-ON defect complex in AlN single crystals," *Physical Review B—Condensed Matter and Materials Physics*, vol. 84, no. 8, p. 081204, 2011.
- [20] W. J. Smith *et al.*, "Nitrogen Vacancies Induce Fatigue in Ferroelectric Al_{0.93}B_{0.07}N," *ACS nano*, 2025.
- [21] X. Yang *et al.*, "N Penetration Enhances Vacancy Filling, Al/Sc-N Bonding, and Ferroelectric Properties in AlScN Films," *IEEE Electron Device Letters*, 2025.
- [22] S. K. Ryoo *et al.*, "Fabrication of Ultrathin Ferroelectric Al_{0.7}Sc_{0.3}N Films under Complementary - Metal - Oxide - Semiconductor Compatible Conditions by using HfN_{0.4} Electrode," *Advanced Materials*, vol. 37, no. 1, p. 2413295, 2025.
- [23] D. Wang *et al.*, "Ferroelectric switching in sub-20 nm aluminum scandium nitride thin films," *IEEE Electron Device Letters*, vol. 41, no. 12, pp. 1774-1777, 2020.
- [24] S. Fichtner *et al.*, "Ferroelectricity in AlScN: switching, imprint and sub-150 nm films," in *2020 joint conference of the IEEE international frequency control symposium and international symposium on applications of ferroelectrics (IFCS-isa)*, 2020: IEEE, pp. 1-4.
- [25] M. Ohring, *Reliability and failure of electronic materials and devices*. Elsevier, 1998.
- [26] J. Suntaranurak, T. Suwanasri, and C. Suwanasri, "Lifetime estimation of switching devices using Weibull distribution analysis," in *2020 17th International Conference on Electrical Engineering/Electronics, Computer, Telecommunications and Information Technology (ECTI-CON)*, 2020: IEEE, pp. 413-416.
- [27] Z. Hu *et al.*, "Demonstration of highly scaled AlScN ferroelectric diode memory with storage density > 100 Mbit/mm²," *arXiv preprint arXiv:2504.13283*, 2025.

- [28] J. X. Zheng *et al.*, "Electrical breakdown strength enhancement in aluminum scandium nitride through a compositionally modulated periodic multilayer structure," *Journal of Applied Physics*, vol. 130, no. 14, 2021.
- [29] P. Wais, "Two and three-parameter Weibull distribution in available wind power analysis," *Renewable energy*, vol. 103, pp. 15-29, 2017.
- [30] S.-M. Chen *et al.*, "Ferroelectricity Engineered AlScN Thin Films Prepared by Hydrogen Included Reactive Sputtering for Analog Applications," in *2024 IEEE Silicon Nanoelectronics Workshop (SNW)*, 2024: IEEE, pp. 29-30.
- [31] J. Zhang, B. Li, J. Zhou, Y. Liu, Y. Hao, and G. Han, "Leakage Study of Ferroelectric AlScN Capacitors Prepared on Different Bottom Electrodes," in *2024 9th International Conference on Integrated Circuits and Microsystems (ICICM)*, 2024: IEEE, pp. 82-86.
- [32] S. Jayatilleka and J. McLinn, "Practical implications of Weibull shape parameter; lessons & pitfalls," in *2021 Annual Reliability and Maintainability Symposium (RAMS)*, 2021: IEEE, pp. 1-6.
- [33] F. Guerin, B. Dumon, and R. Hambli, "Determining the shape parameter of a Weibull distribution from mechanical damage models," in *Annual Reliability and Maintainability Symposium. 2001 Proceedings. International Symposium on Product Quality and Integrity (Cat. No. 01CH37179)*, 2001: IEEE, pp. 156-160.
- [34] E. Y. Wu and R.-P. Vollertsen, "On the Weibull shape factor of intrinsic breakdown of dielectric films and its accurate experimental determination. Part I: theory, methodology, experimental techniques," *IEEE Transactions on Electron Devices*, vol. 49, no. 12, pp. 2131-2140, 2003.
- [35] Y. He *et al.*, "Al_{0.68}Sc_{0.32}N/SiC-based metal-ferroelectric-semiconductor capacitors operating up to 1000° C," *Nano Letters*, vol. 25, no. 12, pp. 4767-4773, 2025.
- [36] Y. Osetsky, M.-H. Du, G. Samolyuk, S. J. Zinkle, and E. Zarkadoula, "Native and radiation induced point defects in AlN and Sc-doped AlN," *Physical Review Materials*, vol. 6, no. 9, p. 094603, 2022.
- [37] C.-W. Lee, N. U. Din, G. L. Brennecke, and P. Gorai, "Defects and oxygen impurities in ferroelectric wurtzite Al_{1-x}Sc_xN alloys," *Applied Physics Letters*, vol. 125, no. 2, 2024.
- [38] I. A. Aleksandrov and K. S. Zhuravlev, "Luminescence line shapes of band to deep centre and donor-acceptor transitions in AlN," *Journal of Physics: Condensed Matter*, vol. 32, no. 43, p. 435501, 2020.
- [39] R. Bulanadi *et al.*, "Interplay between point and extended defects and their effects on jerky domain-wall motion in ferroelectric thin films," *Physical Review Letters*, vol. 133, no. 10, p. 106801, 2024.
- [40] S.-H. Teng, A. Dimou, B. Udofia, M. Ghasemi, M. Stricker, and A. Grünebohm, "Control of ferroelectric domain wall dynamics by point defects: Insights from ab initio based simulations," *Journal of Applied Physics*, vol. 137, no. 15, 2025.
- [41] Q. Zhou *et al.*, "Below bandgap photoluminescence of an AlN crystal: Co-existence of two different charging states of a defect center," *Apl Materials*, vol. 8, no. 8, 2020.
- [42] O. Rehm *et al.*, "Long-Term Stability and Oxidation of Ferroelectric AlScN Devices: An Operando Hard X-ray Photoelectron Spectroscopy Study," *physica status solidi (RRL)–Rapid Research Letters*, vol. 19, no. 3, p. 2400307, 2025.
- [43] M. Li, K. Hu, H. Lin, V. Felmetger, and Y. Zhu, "Oxidation of sputtered AlScN films exposed to the atmosphere," in *2022 IEEE International Ultrasonics Symposium (IUS)*, 2022: IEEE, pp. 1-3.